Journal of Solid State Electrochemistry (2019) 23:3197–3207
https://doi.org/10.1007/s10008-019-04416-0

ORIGINAL PAPER

Synthesis of $MgCo_2O_4$-coated $Li_4Ti_5O_{12}$ composite anodes using co-precipitation method for lithium-ion batteries

Siyong Gu[1] · Chien-Te Hsieh[2,3] · Mohammad Mahmudul Huq[4] · Jo-Pei Hsu[2] · Jianlin Li[5]

Received: 17 January 2019 / Revised: 25 July 2019 / Accepted: 30 September 2019 / Published online: 31 October 2019

Abstract

In the present work, we report synthesis of $MgCo_2O_4$ (MCO)/$Li_4Ti_5O_{12}$ (LTO) composites for Li-ion battery anodes by a co-precipitation method. The objective of this work is to replace expensive Co with Mg and also to exploit advantages of both MCO and LTO. Three samples of MCO/LTO particles with different MCO proportion have various average particle sizes of 38.1, 56.9, and 58.5 nm, confirmed by scanning electron microscopy. Electrochemical studies show that a MCO/LTO anode offers a discharge capacity of ca. 300 mAh g^{-1}, which is two times higher than that achieved by pristine LTO. The MCO/LTO anode also retains 75% of its initial capacity, even if the discharge rate is increased to 5 C. Cyclic stability test reveals that the composite anode still maintains nearly 85.5% of its initial capacity after 150 cycles. Electrochemical impedance spectroscopy indicates that the equivalent series resistance of MCO/LTO electrodes is significantly lower than that of LTO, i.e., from 35.5 to 9.9 Ω. The enhanced performance of the composite electrodes can be attributed to its improved conductivity as well as to the surface modification of LTO particles by MCO nanoparticle deposition which leads to increased number of active sites on the former.

Keywords Lithium-ion battery · Spinel structure · Composite anodes · Magnesium cobaltite · Lithium titanate

Introduction

Demand for more efficient energy storage devices continues increasing [1]. Presently, this demand can potentially be met by lithium-ion batteries (LIBs), which, unlike traditional batteries, have successful application in a large array of electronic devices including portable electronics, electric vehicles (EVs), and solar systems. This success is attributed to their lightweight, much faster charge and discharge capabilities and long cycle life [1–5]. However, electronic devices and EVs are becoming even more energy hungry because of their increased functionality. So, current LIB technology needs even more improvement. The major challenge, nowadays, is to provide high specific energy at low cost without compromising fast charge and discharge capability, and cyclic stability.

Currently, the most popular anode material in commercial sectors is graphite [1, 4]. However, there is concern of lithium plating on graphite anode during fast charging due to the low electrochemical potential of the LiC_6. Other anode materials with higher electrochemical potential can prevent lithium plating, such as is $Li_4Ti_5O_{12}$ (LTO). These issues have been driving researchers to find alternative anode materials [1, 6]. Pristine LTO anode offers superior Li-ion intercalation/deintercalation capability, faster charge and discharge ability, zero-strain volume change during charge and discharge, and better safety performance, compared to the conventional carbon-based anode materials [6–8]. However, LTO suffers from low electric conductivity (*ca.* 5.96×10^{-7} S cm^{-1}) [9], high operating voltage (*ca.* at 1.5 V), and low capacity (175 mAh g^{-1} vs. 372 mAh g^{-1} for graphite), thereby hindering its

✉ Chien-Te Hsieh
cthsieh@saturn.yzu.edu.tw

Jianlin Li
lij4@ornl.gov

1 Fujian Provincial Key Laboratory of Functional Materials and Applications, School of Materials Science and Engineering, Xiamen University of Technology, Xiamen 361024, China

2 Department of Chemical Engineering and Materials Science, Yuan Ze University, Taoyuan 32003, Taiwan

3 Department of Mechanical, Aerospace and Biomedical Engineering, University of Tennessee, Knoxville, TN 37996, USA

4 Department of Chemical and Biological Engineering, University of Saskatchewan, Saskatoon, Canada

5 Energy and Transportation Science Division, Oak Ridge National Laboratory, Oak Ridge, TN 37831, USA

use in high-energy devices [10–12]. To overcome this obstacle, other metal oxides such as TiO_2, SiO_2, SnO_2, ZnO_2, NiO, Fe_3O_4, CuO, and Co_3O_4 have been explored [13–23]. Compared to the other metal oxides, Co_3O_4 and MCo_2O_4 (M = metal) are promising materials with higher theoretical capacity [24, 25]. However, since cobalt is an expensive and toxic material, there have been efforts to partially replace it with naturally abundant and non-toxic materials like Cu, Zn, Fe, Mg, and Mn [26–33].

Recently, $MgCo_2O_4$ (MCO) spinel crystal has attracted interest for energy storage application devices [34–36] and displays high electrical conductivity (ca. 7.51–8.24 × 10^{-4} S cm^{-1}) [37] and high theoretical capacity of 693 mAh/g for LIB anode [31]. Thus far, few groups have studied $MgCo_2O_4$ (MCO) as an anode material, with Chowdari et al. reporting the first use in 2008 [31]. Later, Wang et al. prepared and reported the application of nanowires and nanospheres of MCO [28]. Recently, M. Qin et al. offered an efficient solvothermal route to synthesize Ce- and La-doped LTO composite anode, showing superior electrochemical performance [38]. This work aims to develop a composite anode integrating the merits of high capacity from MCO and excellent cyclability from LTO. The merit of the present work is to explore the robust design of MCO-coated LTO composites, which displayed great prospects as an anode material for Li-ion batteries because of its improved capacity retention, excellent cyclic stability, and low cost.

Experimental

Materials synthesis

Commercially available LTO (purity 99.9%) was purchased from Ubiq Technology Co. (Taoyuan, Taiwan). MCO/LTO composites were synthesized using a co-precipitation method as follows. First, 10 g of LTO was dispersed in 1,000 ml of deionized water followed by adding stoichiometric amount of $Mg(NO_3)_2{\cdot}6H_2O$ and $Co(NO_3)_2{\cdot}6H_2O$ under continuous stirring. Ammonia solution was added dropwise to raise the pH of the solution to 9.0. Finally, H_2O_2 was introduced as a precipitating agent to the solution and stirred for 1 h. The precipitates were filtered from the solution and washed with deionized water to remove all nitrate ions. Then, the obtained powders were dried in a vacuum oven overnight. To obtain MCO/LTO composites, the powders were calcined in air at 500 °C for 5 h. The effects of MCO to LTO proportion were investigated with varying the MCO/LTO weight ratios as 1/10, 2/10, and 3/10, and the samples are designated as M1L1, M1L2, and M1L3 for clarification, respectively, according to MCO to LTO weight ratio.

Materials characterization

The crystalline nature of the as prepared material was studied by X-ray diffraction (XRD) with Cu-Kα radiation using an automated X-ray diffractometer (Shimadzu labx XRD-6000). The XRD scan was carried out within the range of 10–80° at a scan rate of 2° min^{-1}. Rietveld refinement of XRD was carried out using Profex (version 3.11.1). Reference crystallographic data of LTO and MCO were obtained from Crystallography Open Database (http://www.crystallography.net). The microstructure of the materials was observed by a field-emission scanning electron microscope (FE-SEM, JEOL JSM 6701F) and high-resolution transmission electron microscopy (TEM, FEI Talos F200s). The particle size distributions were obtained by counting more than 100 particles on high-resolution SEM pictures. The SEM equipment could provide an automatic scale to measure each particle size. The chemical compositions of the samples were characterized using X-ray photoelectron spectroscopy (XPS), recorded by Fison VG ESCA210 spectrometer with Mg-K_α radiation. The deconvolution of XPS spectra was conducted by a non-linear least squares fitting program with a symmetric Gaussian function.

Electrochemical characterization

Li-ion coin cells with a diameter of 1.5 cm were fabricated in order to study the as prepared anode materials. The schematic diagram for assembling test cells was illustrated in the Electronic Supporting Information (see Figure S1). The electrodes were fabricated according to the following procedure. The slurry was prepared by ball milling active materials (i.e., MCO/LTO composite), conducting additive (i.e., super P, carbon black with an average particle size of 40 nm, Taiwan Maxwave Co., Ltd.), and poly-vinylidenefluoride with the weight ratio of 8:1:1 in N-methyl pyrrolidinone for 3 h. To obtain the uniform slurry, the mixture was blended using a ball mill for 3 h. The slurry was then pasted on a copper foil with a doctor blade controlling a wet thickness of 100 μm, followed by drying using a blow dryer. Half coin cells were assembled with lithium metal as the counter electrode and a polypropylene separator. The mass loading of active material was 25 mg cm^{-2}. The electrolyte was a 1.0 M solution of $LiPF_6$ in ethylene carbonate, polycarbonate, and dimethyl carbonate with a weight ratio of 3:2:5. Cyclic voltammetry was carried out using an electrochemical analyzer (CH Instrument, CHI 608) within a voltage range from 0.5 to 3.0 V at a scan rate of 0.1 mV s^{-1}. The cells were charged at a rate of 0.2 C, and discharged at different constant rates. Basically, C-rate represents a charge or a discharge rate equal to the capacity of a battery in 1 h. Herein, the C-rate calculation was based on the theoretical capacity of LTO (175 mAh g^{-1}). Therefore, 1.0 C is equal to the charge or discharge rate of 175 mA g^{-1}.

Electrochemical impedance spectroscopy (EIS) was performed at open circuit voltage within the frequency range of 100 kHz to 0.01 Hz. The signal amplitude was set at 5 mV. The equivalent circuit was simulated using *Z*-view software.

Results and discussion

The crystal structure of as-prepared LTO and MCO/LTO composites was studied by XRD. As shown in Fig. 1, distinctive diffraction peaks for the pristine LTO sample can be found at 2θ angles of 18.5, 35.7, 43.3, 47.5, 57.3, 62.9, 66.1, 74.4, and 75.5° corresponding to (111), (311), (400), (331), (333), (440), (531), (533), and (622) reflections of $Li_4Ti_5O_{12}$ (JCPDS Card No.: 49-0207), respectively. Basically, this sample displays a single phase of cubic spinel structure with an Fd3m space group. The samples with the presence of MCO show peaks at 2θ angles of 31.0, 36.8, 44.6, 58.9, and 65.2°, which correspond to (220), (311), (400), (511), and (440) planes, respectively, indicating a spinel crystalline structure of $MgCo_2O_4$ (JCPDS Card No.: 02-1073). The intensity of each MCO peak is an increasing function of $MgCo_2O_4$ content. The presence of all major peaks of LTO and MCO confirms successful formation of MCO/LTO composites.

Figure 2 and Table 1 present the Rietveld refinement results using Profex (version 3.11.1). The refinement results confirm that all the peaks of LTO and MCO are well indexed, with the deviation (R_w) reaching as low as < 9.4%. The lattice parameters of both LTO and MCO remain fairly unchanged, suggesting that the original structure of the nanoparticles is not affected during the synthesis process. The average crystallite size of MCO particles can be estimated by the Debye-Scherrer formula:

$$D = k\,\lambda / \left(\beta_{1/2}\cos\theta\right) \quad (1)$$

where D is the crystallite size, k the Scherer constant (0.89), λ the wavelength of the X-ray radiation (0.15406 nm) for Cu-Kα source, θ the Bragg angle, and $\beta_{1/2}$ the full width half maximum of diffraction peak of (311) plane taken at 2θ in radians [39]. Based on the above formula, the average size of the MCO crystallites for M1L2 and M1L1 is 11.7 and 15.0 nm, respectively.

The microstructure of the as-prepared samples was analyzed by FE-SEM and was presented in Fig. 3. Chunk-like pristine LTO particles, as shown in Fig. 3a, are of sizes ranging from 300 to 600 nm. Figure 3b–d shows the aggregated MCO particles deposited on LTO chunks. The particle size distributions of MCO crystals on LTO particles are presented in the form of histograms in Fig. 3e–g. As can be seen, M1L3 sample shows right-skewed distribution. The average particle size of the three samples follows an order: M1L3 (36.1 nm) < M1L2 (56.9 nm) < M1L1 (58.5 nm), clearly showing that the MCO particle size increases with Mg and Co content. The standard deviation for each particle size is approximately 9.6%. The particle size obtained by SEM is larger than that obtained by XRD implies that MCO nanoparticles are composed of smaller monocrystalline primary particles.

TEM micrograph (see Figure S2(a)) displays several MCO crystals in the composite sample. The MCO nanocluster is basically composed of secondary grains, inducing a number of grain boundaries. The selected area diffraction (SAD) pattern from an area focusing on the MCO cluster is given in the inset of Figure S2(a), indicating bright diffraction spots along with diffraction rings. Such ring configuration reveals that the cluster consists of MCO nano-crystallites. Figures S2(b) and S2(c) show the elemental mapping, indicating homogeneous distribution of Co and Mg elements on the MCO crystals.

XPS analysis was performed to investigate surface composition of different MCO/LTO samples. Figure S3(a) shows survey XPS spectra, confirming the presence of MCO content on LTO sample. As expected, the Co/Ti atomic ratio on the MCO/LTO composites obeys an order as M1L3 (0.97) > M1L2 (1.96) > M1L1 (3.11). This increase in the Co/Ti atomic ratio is attributed to more MCO crystals coated on the LTO powders, in accordance with the sequence of the preparation recipe. High-resolution XPS scan on Co 2p of the MCO/LTO samples was illustrated in Figure S3(b–d), confirming the formation of MCO crystals. The Co 2p peaks contain several symmetric peaks, which are composed of overlapping features originating from the $2p_{3/2}$ and $2p_{1/2}$ peaks due to Co^{2+} and Co^{3+} together with the associated satellite structure. The peaks at ca. 782 and 797 eV can be assigned to the presence of Co^{3+}

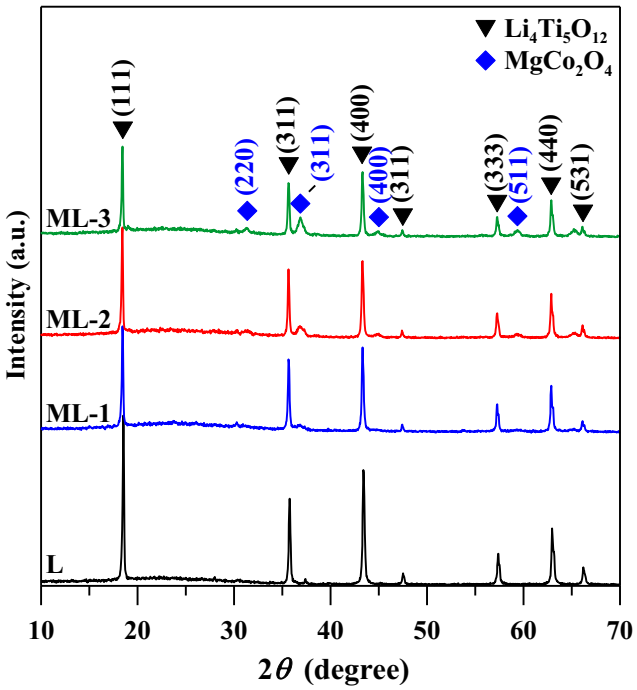

Fig. 1 Typical XRD patterns of different composite anodes

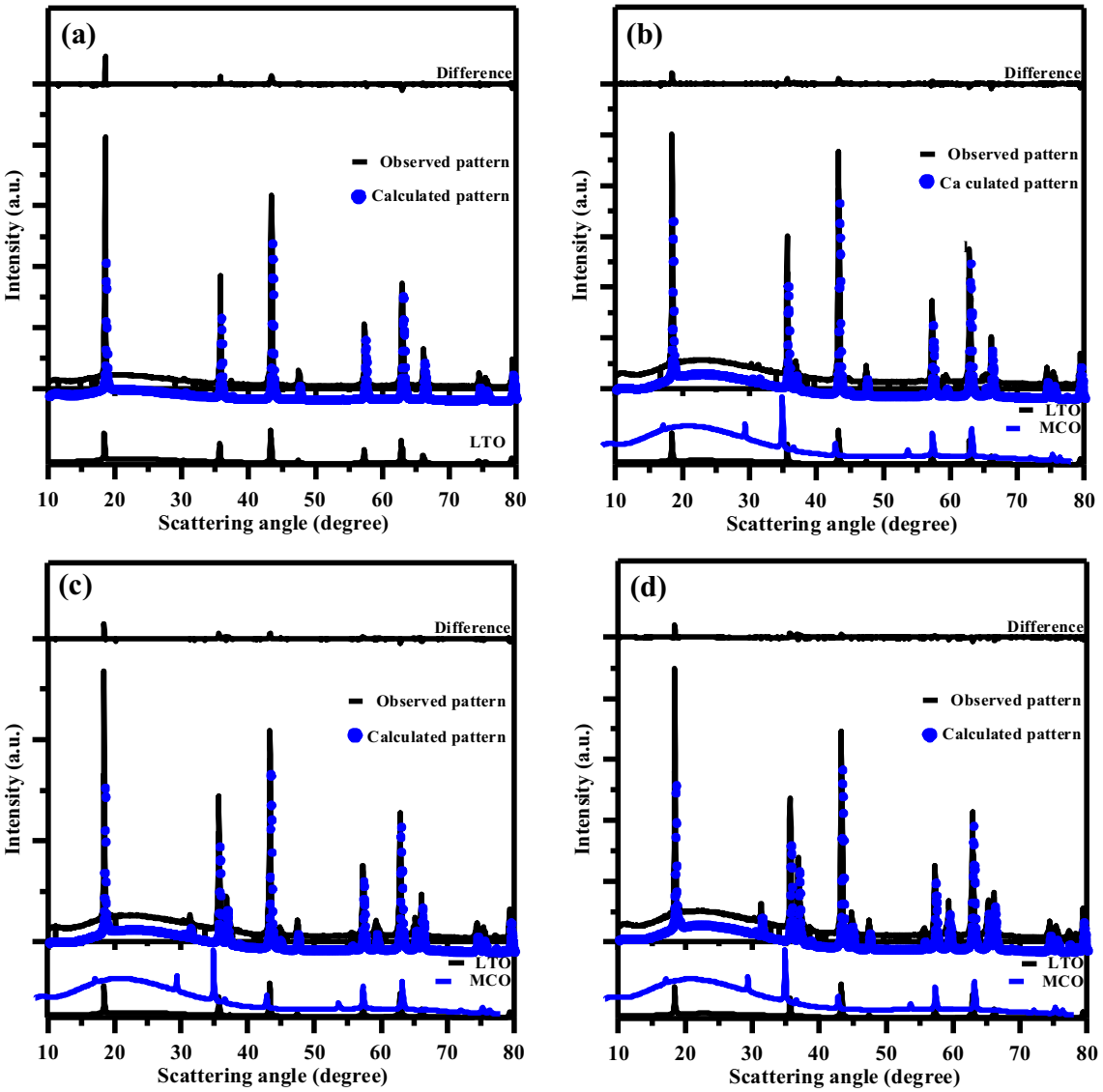

Fig. 2 Results of Rietveld refinement of XRD spectra of **a** L, **b** M1L3, **c** M1L2, and **d** M1L1 sample

component, whereas the peaks at ca. 780 and 796 eV are ascribed to the appearance of Co^{2+} component in $MgCo_2O_4$ crystals [36]. Moreover, the satellite peak at approximately 786–790 eV mainly originates from Co^{2+} species and Co^{3+} component, while the satellite peak located at ca. 803 eV is related to Co^{2+}/Co^{3+} [35, 40, 41]. As a result, the MCO/LTO composite contains pure MCO spinel crystals, which is in good agreement with the results of XRD and XPS analyses.

The cyclic voltammograms (CVs) of pristine L, M1L3, M1L2, and M1L1 electrodes, presented in Figure 4a, b, c, and d, respectively, are carried out at a scan rate of 0.1 mVs^{-1} within the voltage range of 0.5 to 3.0 V vs Li/Li^+. As for sample L, the anodic and cathodic peaks occur at approximately 1.67 and 1.45 V vs Li/Li^+, respectively, characteristic of the redox reaction of LTO. LTO shows no other peaks that suggest any kind of material decomposition. This proves that

Table 1 The lattice parameters of LTO and MCO obtained from the Rietveld refinement

Sample	LTO lattice parameter (Å)	MCO lattice parameter (Å)	R_w (%)	χ^2
L	8.3565	–	9.40	0.0173
M1L3	8.3608	8.0944	6.47	0.0084
M1L2	8.3598	8.1017	7.27	0.0171
M1L1	8.3601	8.0926	7.12	0.0105

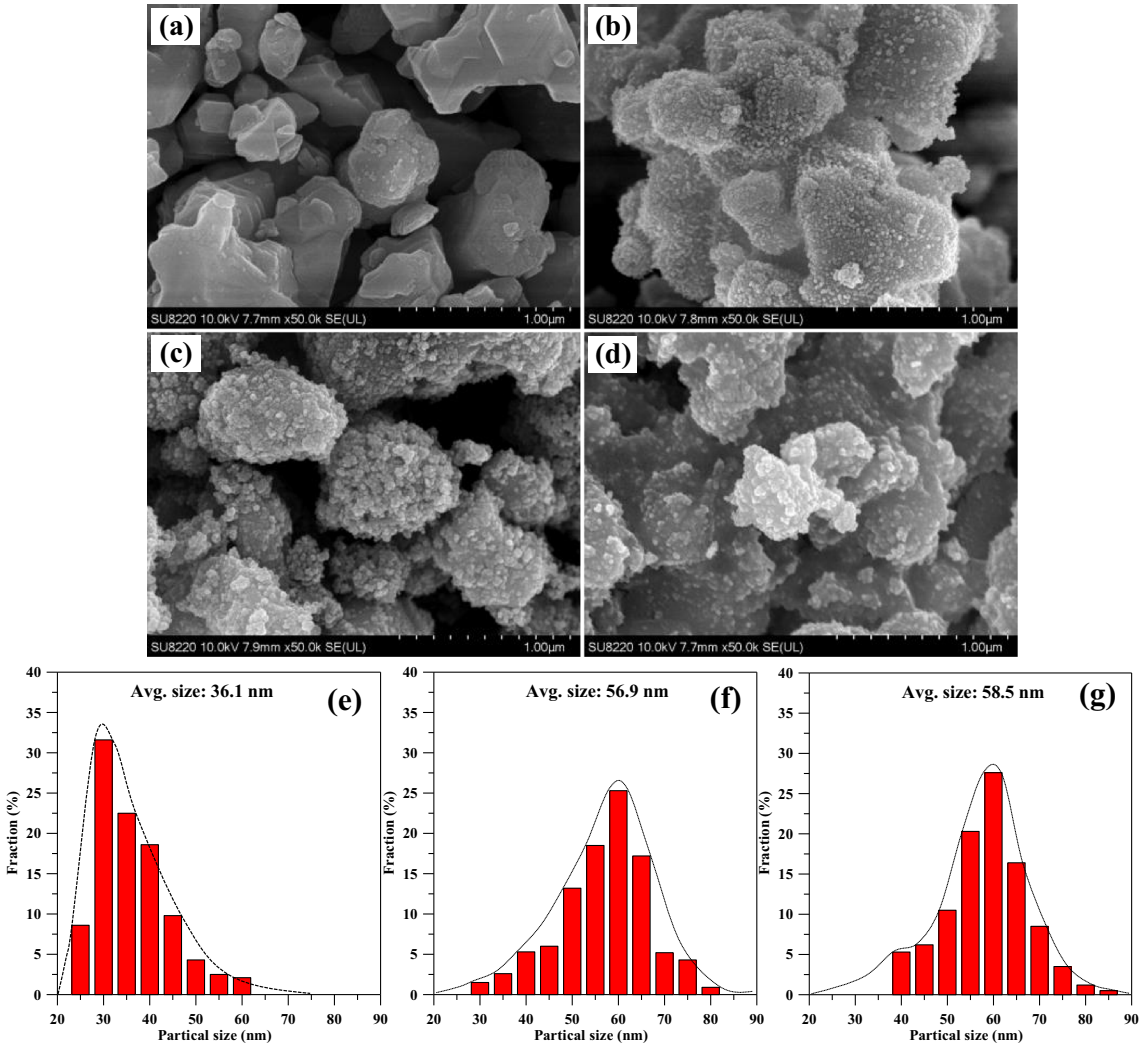

Fig. 3 FE-SEM micrographs of pristine and composite anodes: **a** L, **b** M1L3, **c** M1L2, and **d** M1L1. The particle size distribution of MCO onto LTO powders: **e** M1L3, **f** M1L2, and **g** M1L1

LTO is stable in the above mentioned voltage range, which is also supported by our previous work [39]. The redox reaction step could be expressed as follows:

$$Li_4Ti_5O_{12} + 3e^- + 3Li^+ \leftrightarrow Li_7Ti_5O_{12} \quad \text{(R1)}$$

The reaction step (R1) displays excellent reversibility during Li-insertion/extraction process. In 2008, Y. Sharma et al. proposed that MCO undergoes a reduction reaction during the first discharge to form Li_2O and MgO [28].

$$MgCo_2O_4 + 6Li^+ + 6e^- \leftrightarrow 2Co + 3Li_2O + MgO \quad \text{(R2)}$$

Meanwhile, inactive MgO, which is formed at the first cycle (i.e., (R2)), could remit volume variations effectively during the following electrochemical reactions, resulting in good cycling stability [42]. That is, metal oxide crystals serve as buffering species, effectively limiting the volume expansion and detachment of MCO nanocrystals during the cycling, which has been reported by other literature [43]. After the first cycle, one additional anodic peak appears at 2.01 V vs. Li/Li^+ upon introduction of MCO to LTO, whereas two extra cathodic peaks appear at 0.92 V and 1.19–1.28 V vs. Li/Li^+, as shown in Figure 4b–d. These peaks could be ascribed to the redox reactions described by equation (R3) and (R4) [42].

$$2Co + 2Li_2O \leftrightarrow 2CoO + 4Li^+ + 4e^- \quad \text{(R3)}$$

$$2CoO + 2/3Li_2O \leftrightarrow 2/3Co_3O_4 + 4/3Li^+ + 4/3e^- \quad \text{(R4)}$$

The oxidation/reduction peaks, originated from the redox reactions (i.e., (R3) and (R4)), possibly overlapped at the scan rate. The characteristic peaks of MCO become more pronounced as the MCO proportion increases. Equations (R3) and (R4), appeared within 0.9–1.2 V vs. Li/Li^+, show a redox reversibility of lithium ions in the MCO crystals. Thus, the decoration of MCO nanocrystals induces large number of active sites of Li^+ ion insertion or extraction and reduces the Li^+ ion diffusion resistance, as compared to pristine LTO anode.

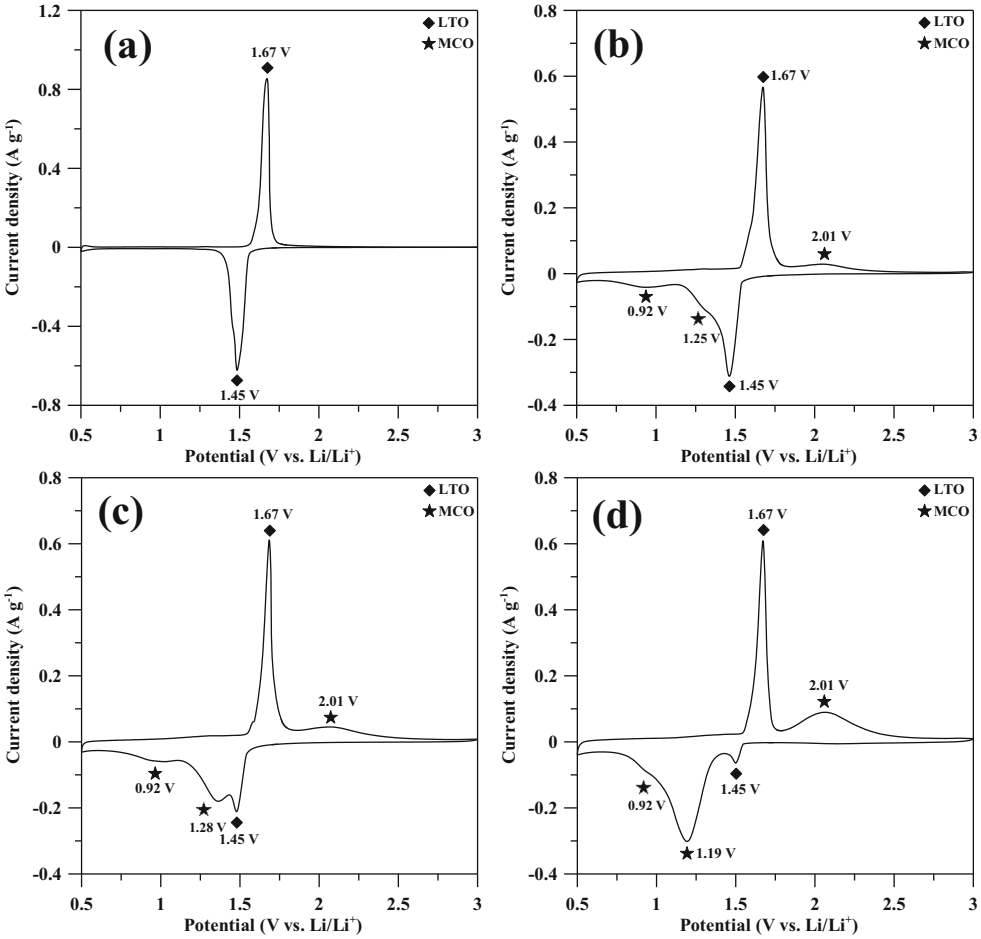

Fig. 4 Typical CV curves of **a** L, **b** M1L3, **c** M1L2, and **d** M1L1 anodes

During the charge-discharge cycling, the MCO is capable of raising the specific capacity of MCO/LTO composite anodes, contributed from the reversible reaction steps, i.e., (R3) and (R4).

Figure 5a, b, c, and d present typical charge-discharge curves of L, M1L3, M1L2, and M1L1 anodes, respectively. The electrochemical test conditions were set at constant discharge rates ranging from 0.1 C to 5 C and a constant charge rate of 0.2 C within the voltage range of 0.5–3.0 V. The charge and discharge process of L sample can be divided into three sections: a rapid voltage drop from 3.0 to 1.5 V, a plateau at 1.5 V, and a second drop from 1.5 to 0.5 V vs Li/Li^+. It is generally recognized that the plateau at 1.5 V is caused by insertion of Li ions into the octahedral sites (16d) of LTO lattice during the intercalation process [39]. At the same time, Li ions located at tetrahedral sites move to octahedral sites (8a). The Li intercalation/de-intercalation process can be expressed by the equation (R5).

$$Li_{3(8a)}[LiTi_5^{4+}]_{(16d)}O_{12(32e)} + 3e^- + 3Li^+ \leftrightarrow Li_{6(16c)}[LiTi_3^{3+}Ti_2^{4+}]_{(16d)}O_{12(32e)} \quad (R5)$$

On the contrary, both M1L2 and M1L1 samples show roughly two plateaus at approximately 1.5 and 1.0 V vs Li/Li^+, corresponding to LTO (R1) and MCO ((R3) and (R4)), respectively. The positions of plateaus are close to that of redox peaks, observed from the CV measurements. It is clear from the figures that the characteristic charge-discharge profiles for MCO become more pronounced as MCO content increases. M1L1 sample shows the highest capacity of ca. 300 mAh g^{-1} at 1 C, almost two times higher than sample L (155 mAh g^{-1} at 0.1 C). The enhanced capacity performance of the MCO/LTO composite can be attributed to the fact that the introduction of MCO offers more active sites for Li^+ storage (i.e., (R3) and (R4)) in the MCO/LTO composite anodes [28]. The specific capacity of the MCO/LTO samples was found to be higher than that of other studies, including TiO_2/LTO (230 mAh g^{-1} at 0.2 C), SnO_2/LTO (224 mAh g^{-1} at 100 mA g^{-1}), and graphene/LTO composite anodes (270 mAh g^{-1} at 25 mA g^{-1}) [43–45]. A comparison of specific capacity between this work and other LTO-based composite anode materials [46–52] was collected, as depicted in Table 2. This table shows that the robust design of MCO/LTO composite anodes delivers a feasibility to replace other LTO-based anode materials for high energy and high power LIBs. Generally, the specific capacity of traditional graphite-like anodes is found to be a decreasing function of C rate due to the presence of ionic diffusion resistance. However, M1L1 and M1L2 still retain 63 and 75% of their initial capacity,

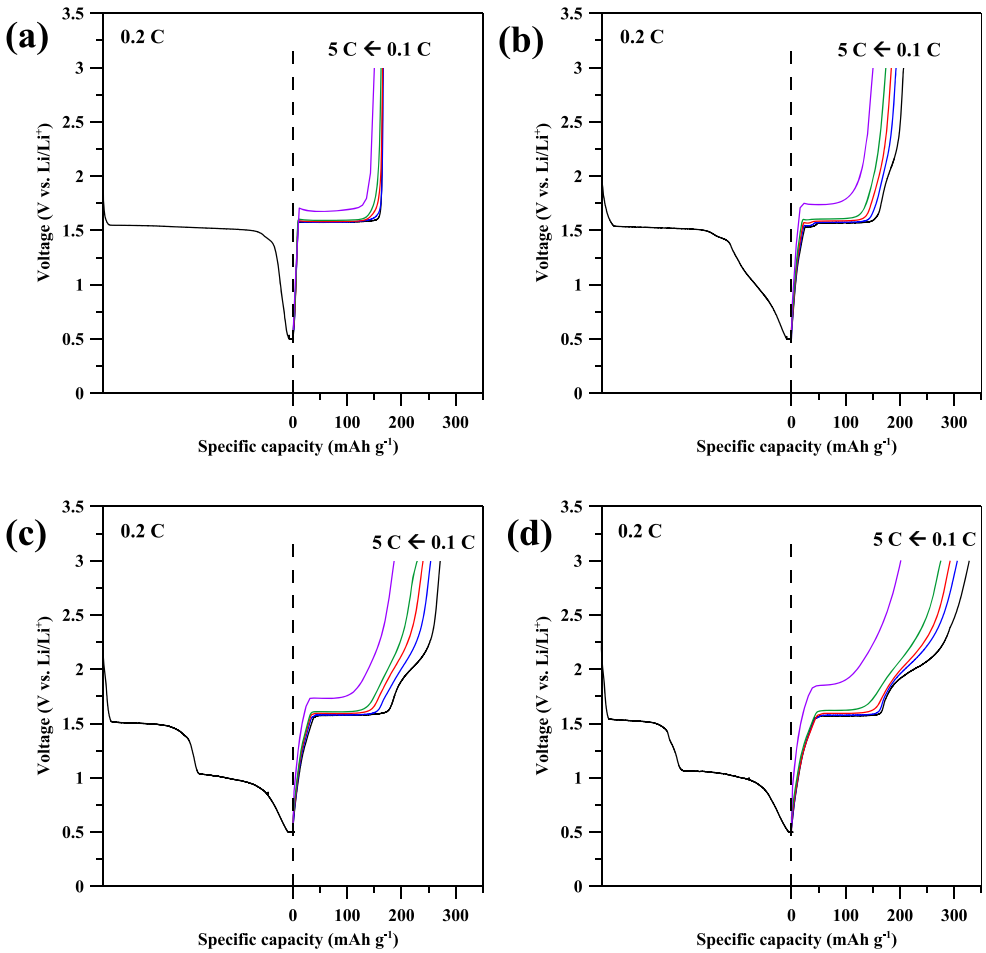

Fig. 5 Typical charge-discharge cycling curves of **a** L, **b** M1L3, **c** M1L2, and **d** M1L1 at 0.1, 0.2, 1, 2, and 5 C rates

respectively even if the discharge rate is increased 50 times from 0.1 to 5 C. The high rate capacity of MCO/LTO composite anodes is superior to traditional graphite anodes, capable of meeting with the requirements of EVs. Based on the above results, it can be concluded that the robust design of MCO/LTO anode satisfies not only high energy density but also high power density.

Figure 6 shows the specific capacity of the as prepared electrode materials over 150 cycles at constant charge and discharge rate of 1 C. The L sample shows a far superior capacity retention ability (ca. 85.4%), likely to be originating from its zero-strain volume change during Li intercalation/de-intercalation. Among the MCO/LTO composite samples, M1L2 anode shows an excellent retention of 85.5%.

Table 2 Comparison of different LTO-based composite anodes for Li-ion batteries

Material	Synthesis method	Performance	Reference
Li_2ZrO_3/LTO	Solid-state reaction	168 mAh g^{-1} at 16 mA g^{-1}	[46]
AlF_3/LTO	Chemical impregnation followed by thermal treatment	163 mAh g^{-1} at 0.2 C	[47]
Ag/LTO	Sol-gel assisted hythermal method	186 mAh g^{-1} at 0.5 C	[48]
ZnO/LTO	Radio magnetron sputtering	293 mAh g^{-1} at 35 mA g^{-1}	[49]
LTO spheres	Hydrothermal process followed by calcination	148 mAh g^{-1} at 0.2 C	[50]
La_2O_3/LTO	Polymeric method followed by calcination	235 mAh g^{-1} at 0.2 C	[51]
Ti_nO_{2n-1}/LTO ($3 < n < 10$)	Sol-gel process followed by heat treatment	171 mAh g^{-1} at 0.2 C	[52]
MCO/LTO	Co-precipitation followed by calcination	300 mAh g^{-1} at 1 C	This work

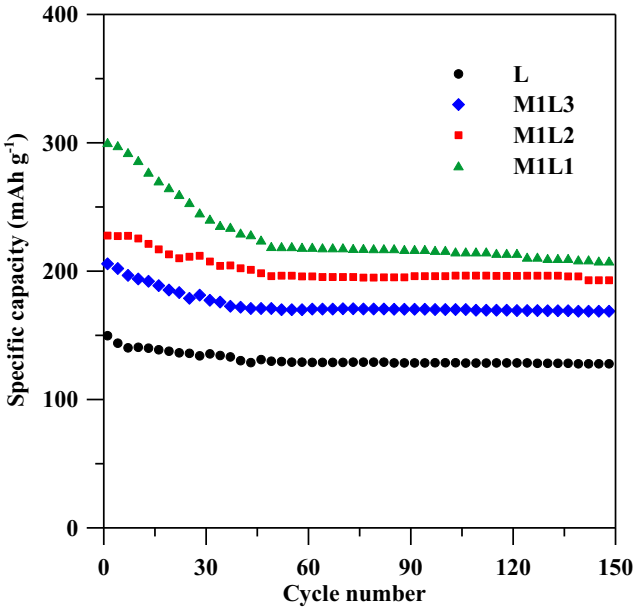

Fig. 6 Cyclic performance of various anodes charged and discharged at 1 C

However, M1L1 experiences a sharp fall in capacity, retaining only 69.1 % of its initial value. The capacity fading of anode materials of LIBs mainly happens due to the volume expansion/contraction during Li ion intercalation/de-intercalation process [28]. Accordingly, the robust design of MCO/LTO composite anode confirms the merits of high capacity from MCO and excellent cyclability from LTO. The capacity loss can also be induced by the side reactions between highly reactive Li metal in the anode, and trace O_2, H_2O, and alkyl carbonate solvents [53]. However, the products of these reactions form a stable film of lithium salts on the electrode at ambient temperature. This film, commonly referred as solid electrolyte interface (SEI) film, prevents further reactions. An interesting finding of this study is that, like the findings of J. E. Hong et al., the capacity decay is strongly related to the MCO content as well as to the size of MCO nanoparticles [10]. The more stable nature of M1L2 can be ascribed to the optimal size of MCO nanoparticles, offering decreased stress between MCO nanoparticles and LTO chunks when volume change happens during Li intercalation/de-intercalation. Therefore, it can be concluded that the cyclic stability of composite anodes could be a function of MCO nanoparticle size. Accordingly, the parameters of co-precipitation synthesis method could be subjected as another topic in controlling particle size and uniformity of MCO nano-crystallites in the near future. Figure 7 shows typical CV curve, charge-

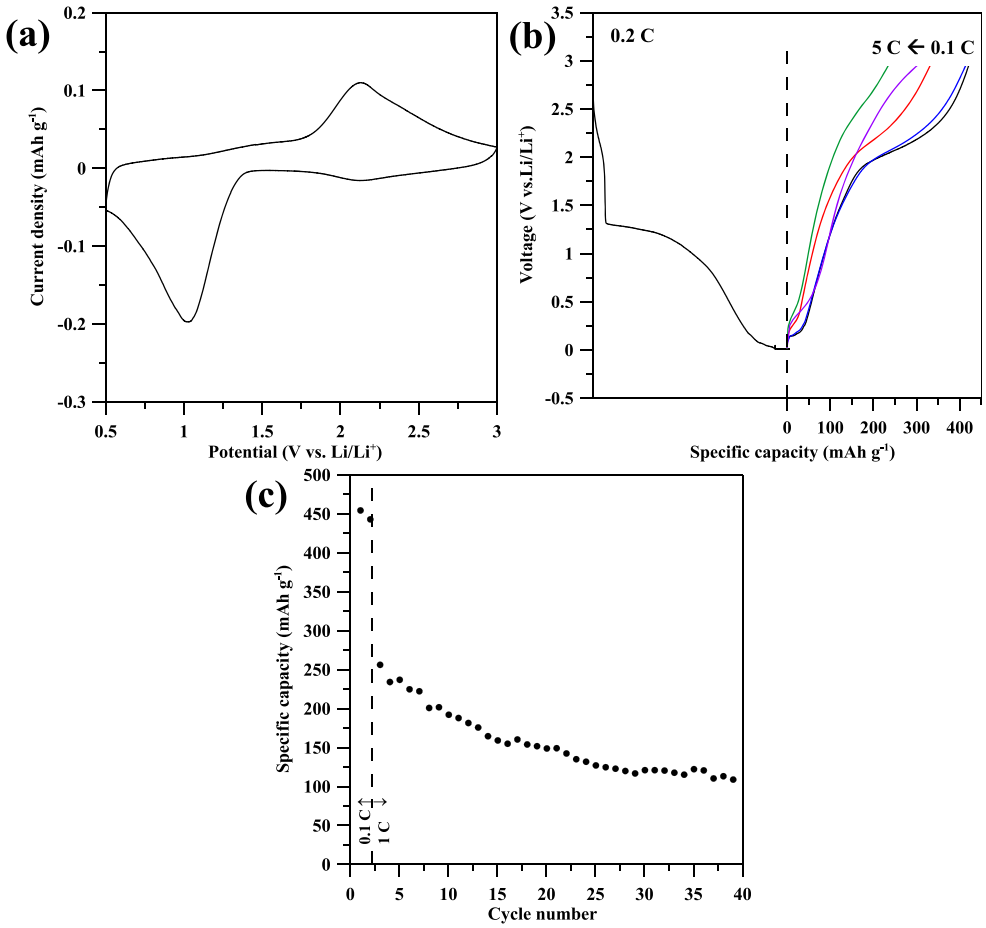

Fig. 7 **a** Typical CV curve of pristine $MgCo_2O_4$ anode. **b** Typical charge-discharge cycling curves of pristine $MgCo_2O_4$ anode at different C rates. **c** Cyclic performance of pristine $MgCo_2O_4$ anode charged and discharged at 1 C

discharge cycling curve, and cyclic performance of pristine $MgCo_2O_4$ anode, showing extremely poor capacity retention ability of pristine MCO (only around 25% of the initial capacity is retained after 40 cycles). We observed from Fig. 7a that the first cathodic peak centered at ~ 1.05 V could be ascribed to the formation of SEI layer, which corresponds to the reduction of Co^{3+} to metallic Co^0 without Mg^{2+} reduction to metallic Mg^0 because of the strong bond energy in MgO [28]. One broad peak centered at around 2.12 V could be ascribed to oxidation of Co to Co^{2+} in the following anodic polarization process, which is identical with previous study [42]. The charge-discharge cycling test (see Fig. 7b and c) reveals that pristine MCO anode displays poor rate capability at high rate and serious capacity fading after potential cycling.

EIS is a widely used tool to estimate the electrical resistance and the behavior of different electrodes in an electrochemical system. Figure 8a shows the Nyquist plots obtained from EIS analysis of as-prepared anodes within the frequency range from 100 kHz to 0.01 Hz. Generally, the Nyquist plot for an electrochemical system can be divided into three major sections: (i) an intersection in the real axis in high frequency region, signifying the bulk resistance of the system, (ii) a semicircle, whose diameter is a measurement of the charge transfer resistance, and (iii) a slant line in the low frequency region, whose slope represents the diffusivity of ions inside the electrode material. A proposed equivalent circuit for simulating the impedance behavior within the frequency region of 100 kHz–10 Hz is presented in Fig. 8b, in which R_S is the bulk

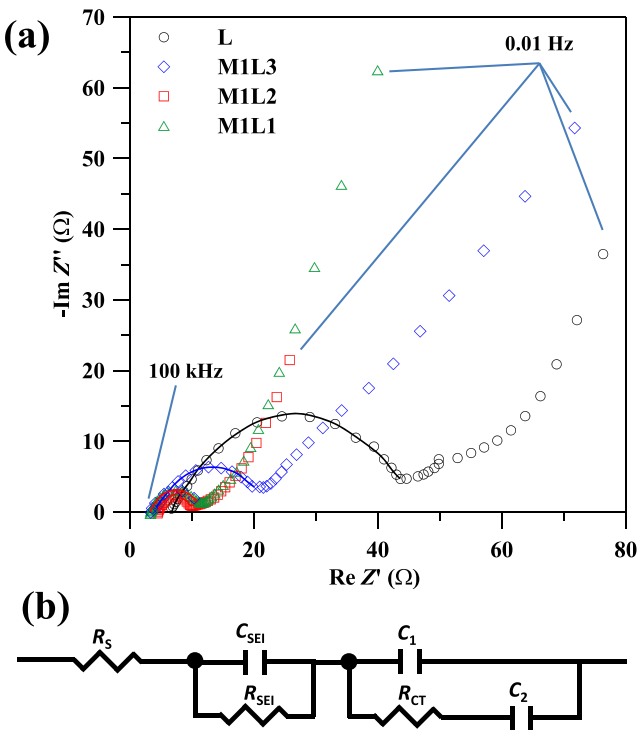

Fig. 8 Electrochemical impedance spectroscopy of composite anodes: **a** Nyquist plot and **b** equivalent serial circuit

Table 3 EIS simulation parameters of different composite anodes

Sample	R_S (Ω)	R_{SEI} (Ω)	R_{CT} (Ω)	R_{ES} (Ω)
L	7.0 (20%)	4.9 (14%)	23.6 (66%)	35.5 (100%)
M1L3	4.3 (21%)	2.5 (12%)	13.3 (67%)	20.1 (100%)
M1L2	4.6 (46%)	1.2 (12%)	4.1 (42%)	9.9 (100%)
M1L1	3.5 (32%)	1.7 (15%)	5.8 (53%)	11.0 (100%)

resistance of the cell, which is a combined resistance of electrode, electrolyte, and separator [54, 55], R_{CT} the charge transfer resistance, and R_{SEI} the resistance of the SEI film. Herein, R_{ES} is the equivalent circuit resistance, representing the sum of R_S, R_{CT}, and R_{SEI}. The fitting results of the equivalent circuit are presented in Table 3, and the solid lines obtained from the simulation (*Z*-view software) were given to compare with the experimental data, as shown in Fig. 8a. The deviation for each component is within 10%. As to all the electrodes, the magnitude of R_{CT} constitutes the major portion of the R_{ES} value. It can be clearly seen from the Nyquist plots as well as from the simulation data that R_{CT} of the MCO/LTO composites are significantly lower than that of pristine LTO. This mainly originates from well dispersed MCO nanocrystals that provide available Li-storage sites over the LTO matrix (i.e., contributed from (R3) and (R4)), leading to small charge transfer resistance. This clearly indicates that introduction of MCO nanoparticles enables easier charge transfer at electrode/electrolyte interface, which partly explains the superior performance of MCO/LTO composites over pristine LTO ones. Overall, this study shows that the MCO/LTO composite is a promising anode material for Li-ion batteries, offering excellent capacity and cyclic stability.

Conclusions

Low capacity of LTO and poor cyclic stability of MCO were dealt with by fabricating a MCO/LTO composite by a co-precipitation method. Electrochemical analysis showed that the introduction of MCO nearly doubles the capacity of LTO anode. The superior performance arises from the formation of MCO active sites on LTO chunks and the improved conductivity of the composite material, proved by EIS analysis. Among all composite samples, M1L2 anode delivered the highest capacity retention (86.1%), which could be ascribed to its optimal MCO particle size. To sum up, the MCO/LTO composites showed a great prospect as an anode material for Li-ion batteries because of its improved capacity retention and cyclic stability, and of course its low cost.

Funding information This study was financially supported by the Ministry of Science and Technology, Taiwan.

References

1. Goriparti S, Miele E, De Angelis F, Di Fabrizio E, Zaccaria RP, Capiglia C (2014) Review on recent progress of nanostructured anode materials for Li-ion batteries. J Power Sources 257:421–423
2. Lou F, Zhou H, Tran TD, Melandsø Buan ME, Vullum-Bruer F, Rønning M, Walmsley JC, Chen D (2014) Coaxial carbon/metal oxide/aligned carbon nanotube arrays as high-performance anodes for lithium ion batteries. ChemSusChem 7:1335–1346
3. Zhao X, Cao M, Hu C (2012) Binder strategy towards improving the rate performance of nanosheet-assembled SnO_2 hollow microspheres. RSC Adv 2:11737–11742
4. Cherian CT, Sundaramurthy J, Reddy MV, Suresh Kumar P, Mani K, Pliszka D, Sow CH, Ramakrishna S, Chowdari BV (2013) Morphologically robust $NiFe_2O_4$ nanofibers as high capacity Li-ion battery anode material. ACS Appl Mater Interfaces 5(20): 9957–9963
5. Winter M, Besenhard JO, Spahr ME, Novák P (1998) Insertion electrode materials for rechargeable lithium batteries. Adv Mater 10:725–763
6. Etacheri V, Marom R, Elazari R, Salitra G, Aurbach D (2011) Challenges in the development of advanced Li-ion batteries: a review. Energy Environ Sci 4:3243–3262
7. Tang Y, Yang L, Qiu Z, Huang J (2009) Template-free synthesis of mesoporous spinel lithium titanate microspheres and their application in high-rate lithium ion batteries. J Mater Chem 19:5980–5984
8. Gao J, Jiang C, Ying J, Wan C (2006) Preparation and characterization of high-density spherical $Li_4Ti_5O_{12}$ anode material for lithium secondary batteries. J Power Sources 155:364–367
9. Vikram Babu B, Vijaya Babu K, Tewodros Aregai G, Seeta Devi L, Madhavi Latha B, Sushma Reddi M, Samatha K, Veeraiah V (2018) Structural and electrical properties of $Li_4Ti_5O_{12}$ anode material for lithium-ion batteries. Results Phys 9:284–289
10. Hong JE, Oh RG, Ryu KS (2015) $Li_4Ti_5O_{12}/Co_3O_4$ composite for improved performance in lithium-ion batteries. J Electrochem Soc 162:A1978–A1983
11. He YB, Li B, Liu M, Zhang C, Lv W, Yang C, Li J, Du H, Zhang B, Yang QH, Kim JK (2012) Gassing in $Li_4Ti_5O_{12}$-based batteries and its remedy. Sci Rep 2:913
12. Guerfi A, Sevigny S, Lagace M, Hovington P, Kinoshita K, Zaghib K (2003) Nano-particle $Li_4Ti_5O_{12}$ spinel as electrode for electrochemical generators. J Power Sources 119:88–94
13. Chen Z, Belharouak I, Sun YK, Amine K (2013) Titanium-based anode materials for safe lithium-ion batteries. Adv Funct Mater 23: 959–969
14. Jiang S, Zhao B, Chen Y, Cai R, Shao Z (2013) $Li_4Ti_5O_{12}$ electrodes operated under hurdle conditions and SiO_2 incorporation effect. J Power Sources 238:356–365
15. Yang KM, Hong YJ, Choi SH, Park BK, Kang YC (2013) Electrochemical properties of $Li_4Ti_5O_{12}$-SnO_2 composite powders prepared by scalable spray drying process. Int J Electrochem Sci 8: 1026–1040
16. Zhou T, Lin Y, Zhao G, Huang Y, Lai H, Li J, Huang Z, Wu SH (2013) The enhancement role of ZnO surface modification on electrochemical performance of $Li_4Ti_5O_{12}$/ZnO composites. Int J Electrochem Sci 8:1316–1327
17. Jiang J, Li Y, Liu J, Huang X, Yuan C, Lou XW (2012) Recent advances in metal oxide-based electrode architecture design for electrochemical energy storage. Adv Mater 24:5166–5180
18. Wang Z, Zhou L (2012) Metal oxide hollow nanostructures for lithium-ion batteries. Adv Mater 24(14):1903–1911
19. Prosini PP, Carewska M, Loreti S, Minarini C, Passerini S (2000) Lithium iron oxide as alternative anode for li-ion batteries. Int J Inorg Mater 2:365–370
20. Ji L, Lin Z, Alcoutlabi M, Zhang X (2011) Recent developments in nanostructured anode materials for rechargeable lithium-ion batteries. Energy Environ Sci 4:2682–2699
21. Opra DP, Gnedenkov SV, Sokolov AA, Zheleznov VV, Voit EI, Sushkov YV, Sinebryukhov SL (2015) Enhancing the reversible capacity of nanostructured TiO_2 (anatase) by Zr-doping using a sol-gel template method. Scr Mater 107:136–139
22. Gnedenkov SV, Opra DP, Kuryavyi VG, Sinebryukhov SL, Ustinov AY, Sergienko VI (2015) Nanostructured TiO_2-$TiOF_2$ composite synthesized by the original method of pulsed high-voltage discharge as anode material for Li-ion battery. Nanotechnol Russ 10(5-6):353–356
23. Gnedenkov SV, Sinebryukhov SL, Zheleznov VV, Opra DP, Voit EI, Modin EB, Sokolov AA, Yu Ustinov A, Sergienko VI (2018) Effect of Hf-doping on electrochemical performance of anatase TiO_2 as an anode material for lithium storage. R Soc Open Sci 5(6):171811
24. Binotto G, Larcher D, Prakash AS, Herrera Urbina R, Hegde MS, Tarascon JM (2007) Synthesis, characterization, and Li-electrochemical performance of highly porous Co_3O_4 powders. Chem Mater 19:3032–3040
25. Yan N, Hu L, Li Y, Wang Y, Zhong H, Hu X, Kong X, Chen Q (2012) Co_3O_4 nanocages for high-performance anode material in lithium-ion batteries. J Phys Chem C 116:7227–7235
26. Sharma Y, Sharma N, Subba Rao GV, Chowdari BV (2007) Nanophase $ZnCo_2O_4$ as a high performance anode material for Li-ion batteries. Adv Funct Mater 17:2855–2861
27. Mondal AK, Su D, Chen S, Xie X, Wang G (2014) Highly porous $NiCo_2O_4$ nanoflakes and nanobelts as anode materials for lithium-ion batteries with excellent rate capability. ACS Appl Mater Interfaces 6(17):14827–14835
28. Wang X, Zhai G, Wang H (2015) Facile synthesis of $MgCo_2O_4$ nanowires as binder-free flexible anode materials for high-performance Li-ion batteries. J Nanopart Res 17:339
29. Sharma Y, Sharma N, Rao GS, Chowdari BV (2007) Lithium recycling behaviour of nano-phase-$CuCo_2O_4$ as anode for lithium-ion batteries. J Power Sources 173:495–501
30. Luo W, Hu X, Sun Y, Huang Y (2012) Electrospun porous $ZnCo_2O_4$ nanotubes as a high-performance anode material for lithium-ion batteries. J Mater Chem 22:8916–8921
31. Sharma Y, Sharma N, Rao GS, Chowdari BV (2008) Studies on spinel cobaltites, $FeCo_2O_4$ and $MgCo_2O_4$ as anodes for Li-ion batteries. Solid State Ionics 179:587–597
32. Li J, Wang J, Liang X, Zhang Z, Liu H, Qian Y, Xiong S (2013) Hollow $MnCo_2O_4$ submicrospheres with multilevel interiors: from mesoporous spheres to yolk-in-double-shell structures. ACS Appl Mater Interfaces 6:24–30
33. Shen L, Che Q, Li H, Zhang X (2014) Mesoporous $NiCo_2O_4$ nanowire arrays grown on carbon textiles as binder-free flexible electrodes for energy storage. Adv Funct Mater 24:2630–2637
34. Okamoto S, Ichitsubo T, Kawaguchi T, Kumagai Y, Oba F, Yagi S, Shimokawa K, Goto N, Doi T, Matsubara E (2015) Intercalation and push-out process with spinel-to-rocksalt transition on Mg insertion into spinel oxides in magnesium batteries. Adv Sci 2: 1500072
35. Gu S, Hsieh CT, Huq MM, Hsu JP, Ashraf Gandomi Y, Li J (2019) Preparation of $MgCo_2O_4$/graphite composites as cathode materials for magnesium-ion batteries. J Solid State Electrochem 7:1–9
36. Guan X, Wang Q, Luo P, Yu Y, Li X, Zhang Y, Chen D (2018) Morphology-tuned synthesis of $MgCo_2O_4$ arrays on graphene coated nickel foam for high-rate supercapacitor electrode. Int J Electrochem Sci 13:2272–2285
37. Kamioka N, Ichitsubo T, Uda T, Imashuku S, Taninouchi Y, Matsubara E (2008) Synthesis of spinel-type magnesium cobalt oxide and its electrical conductivity, Mater. Transactions 49:824–828

38. Qin M, Li Y, Lv XJ (2017) Preparation of Ce-and La-doped $Li_4Ti_5O_{12}$ nanosheets and their electrochemical performance in Li half cell and $Li_4Ti_5O_{12}$/$LiFePO_4$ full cell batteries. Nanomaterials 7:150
39. Hsieh CT, Lin JY (2010) Influence of Li addition on charge/discharge behavior of spinel lithium titanate. J Alloys Compd 506:231–236
40. Stelmachowski P, Maniak G, Kaczmarczyk J, Zasada F, Piskorz W, Kotarba A, Sojka Z (2014) Mg and Al substituted cobalt spinels as catalysts for low temperature deN_2O-evidence for octahedral cobalt active sites. Appl Catal B Environ 146:105–111
41. Pu ZY, Zhou H, Zheng YF, Huang WZ, Li XN (2017) Enhanced methane combustion over Co_3O_4 catalysts prepared by a facile precipitation method: effect of aging time. Appl Surf Sci 410:14–21
42. Wang F, Liu Y, Zhao, Wang Y, Wang Z, Zhang W, Ren F (2018) Facile synthesis of two-dimensional porous $MgCo_2O_4$ nanosheets as anode for lithium-ion batteries. Appl Sci 8:22
43. Zhou GM, Wang DW, Li F, Zhang LL, Li N, Wu ZS, Wen L, Lu GQ, Cheng HM (2010) Graphene-wrapped Fe_3O_4 anode material with improved reversible capacity and cyclic stability for lithium ion batteries. Chem Mater 22:5306–5313
44. Yuan T, Tan Z, Ma C, Yang J, Ma ZF, Zheng S (2017) Challenges of spinel $Li_4Ti_5O_{12}$ for lithium-ion battery industrial applications. Adv Energy Mater 7:1601625
45. Zhao B, Ran R, Liu M, Shao Z (2015) A comprehensive review of $Li_4Ti_5O_{12}$-based electrodes for lithium-ion batteries: the latest advancements and future perspectives. Mater Sci Eng R 98:1–71
46. Zhang H, Liu Y, Wang T, Yang Y, Shi S, Yang G (2016) Li_2ZrO_3-coated $Li_4Ti_5O_{12}$ with nanoscale interface for high performance lithium-ion batteries. Appl Surf Sci 368:56–62
47. Liang G, Pillai AS, Peterson VK, Ko KY, Chang CM, Lu CZ, Liu CE, Liao SC, Chen JM, Guo Z, Pang WK (2018) Effect of AlF_3-coated $Li_4Ti_5O_{12}$ on the performance and function of the $LiNi_{0.5}Mn_{1.5}O_4$||$Li_4Ti_5O_{12}$ full battery-an in-operando neutron powder diffraction study. Front Ener Res 6:1–12
48. Li J, Huang S, Xu S, Lan L, Lu L, Li S (2017) Synthesis of spherical silver-coated $Li_4Ti_5O_{12}$ anode material by a sol-gel-assisted hydrothermal method. Nanoscale Res Lett 12:576
49. Wang Y, Ren Y, Dai X, Yan X, Huang B, Li J (2018) Electrochemical performance of ZnO-coated $Li_4Ti_5O_{12}$ composite electrodes for lithium-ion batteries with the voltage ranging from 3 to 0.01 V. R Soc Open Sci 5:180762
50. Wang L, Zhang Y, Scofield ME, Yue S, McBean C, Marschilok AC, Takeuchi KJ, Takeuchi ES, Wong SS (2015) Enhanced performance of "flower-like" $Li_4Ti_5O_{12}$ motifs as anode materials for high-rate lithium-ion batteries. ChemSusChem 8(19):3304–3313
51. Wei A, Li W, Zhang L, Liu Z (2017) Enhanced electrochemical performance of La_2O_3-modified $Li_4Ti_5O_{12}$ anode material for Li-ion batteries. In IOP Conference Series: Materials Science and Engineering (231(1):012082). IOP Publishing
52. Zhang X, Xu W, Liu W, Li X, Zhong X, Lin Y (2018) Ti_nO_{2n-1}-coated $Li_4Ti_5O_{12}$ composite anode material for lithium-ion batteries. JOM 70(8):1383–1386
53. Yang CR, Wang YY, Wan CC (1998) Composition analysis of the passive film on the carbon electrode of a lithium-ion battery with an EC-based electrolyte. J Power Sources 72:66–70
54. Churikov AV, Ivanishchev AV, Ivanishcheva IA, Zapsis KV, Gamayunova IM, Sycheva VO (2008) Kinetics of electrochemical lithium intercalation into thin tungsten (VI) oxide layers. Russ J Electrochem 44(5):530–542
55. Gao Z, Zhang X, Hua H, Guo D, Zhao H, Yu H (2017) Influencing factors of low- and high-temperature behavior of Co-doped Zn_2SnO_4-graphene-carbon nanocomposite as anode material for lithium-ion batteries. J Electroanal Chem 791:56–63